Journal of MATERIALS RESEARCH

Article
DOI:10.1557/s43578-023-00956-4

Optimal synthesis, fine-scale microstructural characterization, and property estimation of reactive-spark plasma sintered bulk multicomponent (Nb, Ti, Zr, Cr)B_2

Rahul Mitra[1], Taraknath Maity[1], Nidhi Sharma[1], Khushubo Tiwari[1], Tanmoy Maiti[1], Krishanu Biswas[1,a)]

[1] Department of Materials Science and Engineering, Indian Institute of Technology Kanpur, Kanpur 208016, India
[a)] Address all correspondence to this author. e-mail: kbiswas@iitk.ac.in

Received: 28 September 2022; accepted: 9 February 2023; published online: 13 March 2023

Gradual evolution of bulk equimolar (Nb, Ti, Zr, Cr)B_2 was studied via boro-carbothermal reduction of metal oxides with varying B_4C content (0.45 mol–0.75 mol) at 1800 °C for 75 min, adopting single-stage reactive spark plasma sintering scheme. The phase evolution and microstructural investigation revealed almost fully formed high-entropy boride (HEB) phase for B_4C content of 0.7 mol with a small amount of retained phases; graphite, Cr_2O_3, and intermittent $Nb_{0.8}Zr_{0.2}C$. The HEB phase in the sintered specimens exhibits hardness up to 37 GPa with elastic modulus up to 415 GPa, depending on the B_4C content in the pre-mix. The sintered specimen's thermal conductivity increases with temperature, attaining 28 W/m K at 1600 °C. Thermodynamic and diffusion calculations reveal that the boro-carbothermal reaction between oxides yields individual metal borides, which are then interdiffused to form the HEB phase. The unique methodology is expected to serve as a promising route for obtaining multicomponent diborides.

Introduction

The advancement in material science and technology has taken a leap forward with the development of high-entropy ceramics (HECs), an emerging class of multicomponent materials. Similar to high-entropy alloys (HEAs) [1–9], these materials can also be stabilized at higher temperatures due to the high configurational entropy effect [8]. Several research groups have reported [10] the synthesis and characterization of various types of HECs: oxides [11, 12], nitrides [13], silicides [14, 15], carbides [16–19], and diborides [8, 10, 20–25], chalcogenides [26], etc., in the bulk as well as thin film. Among these classes of materials, high-entropy diborides (HEBs) exhibit a unique combination of physio-thermo-mechanical properties including high melting temperature (> 3000 °C), high hardness (22.5–28.3GPa), relatively higher fracture toughness (4.47 ± 0.40 MPa $m^{1/2}$), chemical inertness, resistance to wear and corrosion, good electrical and thermal conductivities, etc., as compared to other HECs [20–22]. In recent literature, the processing of the HEB phases (both in powder and in bulk form) through different methods has widely been discussed. Gild et al. [8] reported, for the first time, the synthesis of bulk HEBs with a sinter density of ~ 92% was processed at 2000 °C for 5 min. under 30 MPa pressure in vacuum via spark plasma sintering of the mechanically milled powder mixtures of several individual diborides. The as-sintered HEBs exhibited a hardness of ~ 22.5 GPa with excellent oxidation resistance as compared to the individual diborides under similar conditions. Tallarita et al. [23] developed bulk HEBs $(Hf_{0.2}Mo_{0.2}Ta_{0.2}Nb_{0.2}Ti_{0.2})B_2$ ceramic via a combination of self-propagating high-temperature synthesis (SHS) route and the SPS, at a temperature of 1950 °C. Nevertheless, the primary obstacle for fabricating HEBs was still the difficulties of densification and the related impurity incurred by the manufacturing process, albeit some oxide impurities were discovered. Thus, boro-carbothermal reductions of metal oxides have been suggested as an efficient, feasible, and inexpensive strategy in this time of need. Natural elemental oxides are more abundant and easily available; therefore, the conversion of mixed oxides into diborides is a feasible way to synthesize them. In this regard,

several researchers have reported boro-carbothermal reduction (BCTR) of transition metal oxides by B_4C and C for the synthesis of single-phase diborides [24, 25, 27, 28]. Zhang et al. [24] developed $(Hf_{0.2}Mo_{0.2}Ta_{0.2}Nb_{0.2}Ti_{0.2})B_2$ using BCTR of the corresponding metal oxides at 2000 °C and achieved a sinter density of ~ 98.5%. They reported that the sintered HEB showed an improved hardness of ~ 27 GPa and fracture toughness of ~ 4.47 MPa $m^{-1/2}$. Gu et al. [25] designed a BCTR route for the synthesis of HEB powders from oxide by adjusting B_4C/MO_x (where MO_x = transition metal oxides) and studied the densification behavior of the as-prepared powders. Feng et al. [27] investigated the production of high-purity $(Hf_{0.2}Zr_{0.2}Ti_{0.2}Ta_{0.2}Nb_{0.2})B_2$ powders with fine particle size using a two-step procedure including BCTR and solid solution formation. Further literature survey also reveals that boron carbide is an effective reducing agent for metal oxides [29–33] for the preparation of phase pure HEBs. Earlier reports on the boro-carbothermal approach for multicomponent diborides involved powder preparation and densification in two steps [30–32]. To promote the boro-carbothermal reaction, the powder is prepared in a vacuum furnace at 1600°–1650 °C at 10 °C/min for 60 min followed by sintering at 1900–2100 °C for 10–15 min. This limits the synthesis time of the bulk component. Therefore, a modified approach for fabricating bulk components in a single step is much needed. In addition to that, the research on HEBs has been more focused on the prime refractory diborides, i.e., HfB_2, ZrB_2, NbB_2, TiB_2, TaB2, MoB_2, and WB_2 [8, 20–25, 27, 29–32]. To date, most researches have been done on the $(Hf_{0.2}Zr_{0.2}Ti_{0.2}Ta_{0.2}Nb_{0.2})B_2$ system. It has been observed that the sinterability and properties of HEBs are also affected by their composition [32]. Therefore, it is crucial to study HEBs with a variety of components.

In this context, we present the synthesis route of high-entropy borides of quaternary composition from a mixture of metal oxides and boron carbide using a boro-carbothermal reduction at a lower temperature (1800 °C) and duration (75 min). In situ reactive spark plasma sintering is used to achieve the boro-carbothermal reduction and densification in a single stage. In this inventive step, the formation of the multicomponent diboride and the densification takes place simultaneously without undergoing any intermediate processing steps, thus saving an ample amount of time. Further, as a reference, we used a novel HEB composition of (Nb, Ti, Zr, Cr)B_2. The synthesizability of the bulk equimolar diboride of composition (Nb, Ti, Zr, Cr)B_2 was first theoretically investigated using detailed thermodynamic calculations of the possible chemical reactions between constituent oxide mixtures and boron carbide (B_4C). Consequently, the effect of varying B_4C content (in mol) on the yield of high-entropy boride is also investigated using XRD and SEM. The final phase composition and residual products were analyzed using transmission emission microscopy (TEM). The basic mechanical (hardness and elastic modulus) and thermal properties (thermal conductivity) of the consolidated pellet have been measured and reported. Attempts have been made to explain the formation of the solid solution diborides from the individual diborides by a detailed thermodynamic calculation as well as diffusion kinetics during boro-carbothermal reduction of metal oxide by B_4C. In a nutshell, the present study is expected to provide a deep insight into synthesizing multicomponent diborides through in situ boro-carbothermal reductions of oxide mixtures.

Results

Phase analysis and evolution of solid solution phase

Figure 1(a) shows the XRD patterns of the bulk samples sintered at 1800 °C for holding times of 75 min. In addition, the XRD pattern of as-milled HB5 powder is also shown in Figure S1a (Supplementary Information-II), indicating that all the reactant powders, i.e., oxides and boron carbides, have been present in this mixture. The XRD patterns in Fig. 1(a) indicate the gradual emergence of peaks due to a high-entropy/multicomponent diboride or high-entropy boride phase (referred to as HEB, as in high-entropy boride) upon sintering the oxide-mix with varying boron carbide content. In fact, the sintered samples exhibit the presence of intense peaks corresponding to the HEB phase ($a = b = 0.3056$ nm, $c = 0.3255$ nm, space group P6/mmm). However, consistent presence of some peaks due to oxide phases can also be observed in HB1 to HB4 samples. These peaks correspond to oxide phases include $Nb_{0.8}Ti_{0.2}O_2$ ($a = b = 1.356$ nm, $c = 0.599$ nm; space group I41/a, ICDD ref. 04-020-5522), $CrNbO_4$ ($a = 0.465$ nm, $b = 0.465$ nm, $c = 0.301$ nm; space group P42/mnm, ICDD ref. 04-002-1851) and ZrO_2 ($a = 0.517$ nm, $b = 0.523$ nm, $c = 0.534$ nm; space group P21/c, ICDD ref. 04-013-6952). Interestingly, XRD peaks arising from these oxides are found to be significantly diminished upon increasing B_4C content by more than 0.6 mol (see XRD patterns of HB4, HB5, and HB6). For HB5, additional oxide phases cannot be found in the XRD pattern. The presence of several constituent diboride phases (both elemental and binary diborides) such as TiB_2 (ICDD ref. 04-002-0799), $Ti_{0.5}Zr_{0.5}B_2$ (ICDD ref. 04-011-7056), $Nb_{0.5}Ti_{0.5}B_2$ (ICDD ref. 04-011-7058), $Nb_{0.5}Cr_{0.5}B_2$ (ICDD ref. 04-018-7963), and $Nb_{0.5}Zr_{0.5}B_2$ (ICDD ref. 04-011-7060) can be detected in the patterns which can be indexed by matching them from the Pearson crystal database (PCD). There are also a few peaks of residual B_4C in the XRD pattern of the HB6 sample, suggesting that the boro-carbothermal reduction of oxides may have been successful with a boron carbide content of less than 0.75 mol. A detailed discussion of peak evolution during XRD is discussed in S1, Supplementary Information-I.

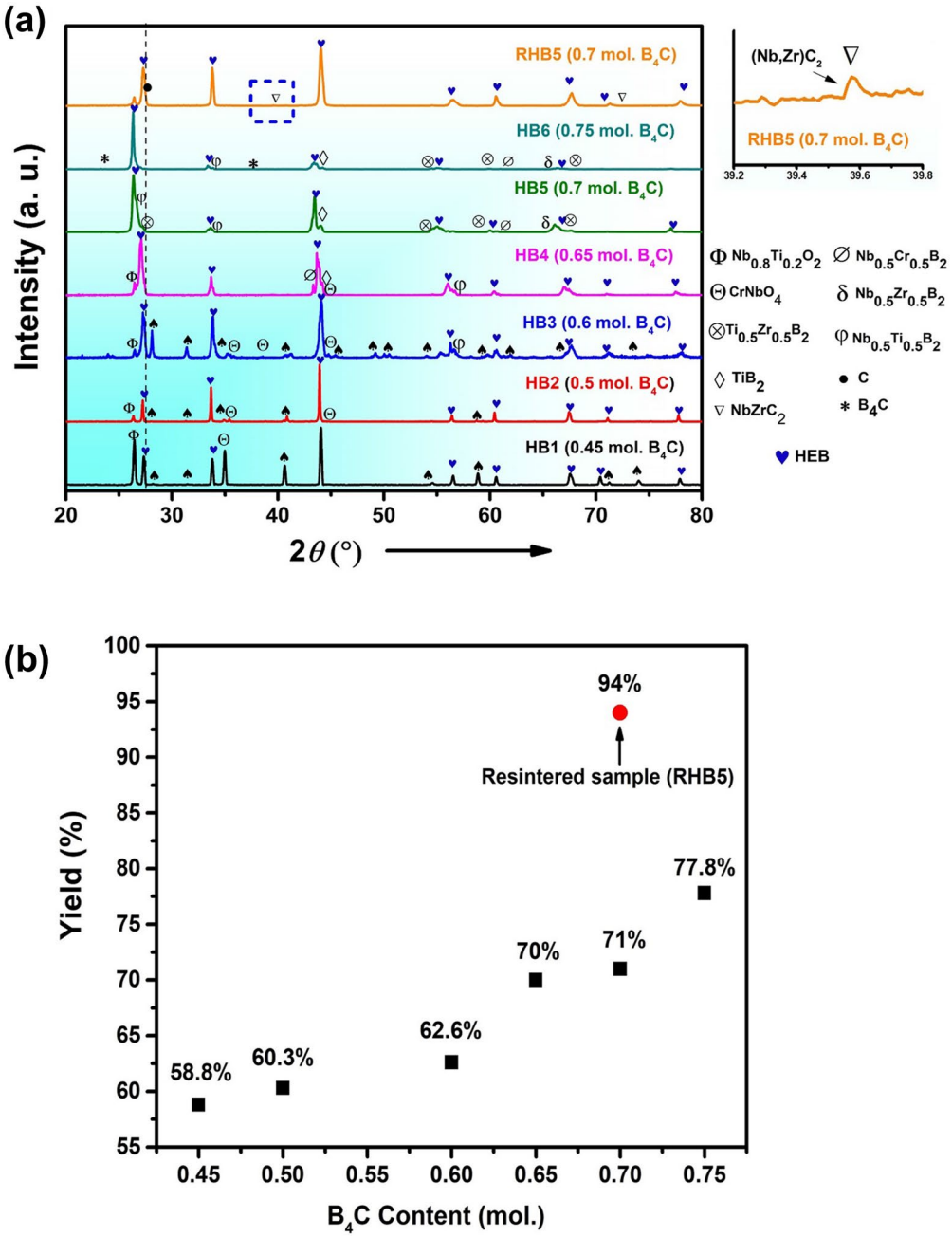

Figure 1: (a) XRD patterns of the spark plasma sintered pellets revealing the evolution of the high-entropy boride (HEB) phase formed via boro-carbothermal reaction with various concentrations of boron carbide (B_4C); (b) percentage yield of the HEB phase estimated from the XRD patterns.

A thorough inspection of XRD peaks corresponding to the HEB phase in the sintered samples (HB1 to HB6) reveals a considerable shift in the peak position to the lower angles [from 2θ = 27.37° to 26.34°, corresponding to (001)], indicating an increase in the c-axis (3.5%) of the hexagonal HEB phase. This is possibly due to the variation in the M–B bond length (M = Metal, B = Boron) since it is likely that different metal atoms are randomly occupying the basal plane of the high-entropy lattice throughout the evolution of the HEB phase [21]. Although a marginal difference in the a-axis has been observed in the estimated values (< 1%)., it is particularly noteworthy that the intensity of the diffraction peak corresponding to the (100) plane is particularly weak in the case of HB4, HB5, and HB6 samples. This can be explained from the viewpoint of occupancy of individual Wyckoff's position in a crystal. If all the Wycoff's positions in the crystal are inadequately occupied by the required number of atoms, it can lower the value of the atomic structure factor, which might lead to a decrease in the

intensity. The phase percentage of the HEB phase has been estimated from the intensity ratio of the XRD peaks as shown in Fig. 1(b). Figure 1(b) shows that the phase percentage or volume fraction of the HEB phase in the sintered specimens increased from 58.8% in HB1 to 77.8% in the HB6 sample. This suggests that increasing B_4C content in the as-milled mixture can significantly help in the completion of boro-carbothermal reactions.

The phase percentage of the HEB phase in the sintered compact can further be increased by resintering the HB5 sample. To facilitate further interdiffusion between the constituent diborides, the single sintered pellet of HB5 was crushed in an agate mortar and the crushed powder was further sintered at 1800 °C for 75 min (achieved density of 4.77 g/cc). The XRD pattern of RHB5 as shown in Fig. 1(a) (the top-most pattern) reveals the appearance of the prominent peaks due to the HEB phase ($a = b = 0.3073$ nm, $c = 0.3304$ nm; space group P6/mmm) along with a few low-intensity peaks of carbon and (Nb, Zr) C_2 (ICDD ref. 04-001-5862). In comparison with the conventional ZrB_2 and HfB_2-based materials, the reduction of lattice parameters can be attributed to the incorporation of the smaller size of Nb, Cr, and Ti than Zr and Hf. However, any peaks corresponding to oxide phases could not be detected. The RHB5 specimen reveals an increment in the phase percentage of the HEB phase up to 94% due to resintering. The detailed evolution of the HEB phase upon resintering is discussed in S2, Supplementary Information-I.

Microstructural investigations

Morphology and compositional analysis

The cross-sectional BSE-SEM micrographs obtained from the as-sintered samples are reported in Fig. 2. The microstructures disclose the morphological features of the sintered compacts, revealing the presence of distinct phases, which are highlighted on the micrographs. The light gray contrast regions (marked by yellow arrows) correspond to the HEB phase. The bright contrast regions (marked by red arrows) in HB1 to HB6 samples show different oxide-rich phases corresponding to Nb/Ti–rich oxides, Cr-rich oxides, and ZrO_2. Incidentally, in the HB2 sample, a few Ti–rich zones can be detected which are separately marked with black dotted circles. The corresponding SEM–EDS elemental map of HB2 and HB3 is shown in Figure S2a-b, Supplementary Information-II. It is particularly noteworthy to mention that loosely compacted phases (as denoted by a blue dotted box) can be observed within the oxide regions in the majority of the microstructures. These areas are possibly corresponding to the reaction zones where the presence of oxide-rich phases is evident. These regions are more prominent in the case of the compacts, which are sintered from those oxide mixes in which B_4C content is < 0.7 mol. Interestingly, the oxide-rich regions are found to disappear in the case of the HB5 sample. This gradual disappearance of the residual oxide phases can also be attributed to the near completion of the boro-carbothermal reduction of oxides upon increasing B_4C content in the powder mixture. However, a traceable amount of oxide phases (mainly ZrO_2, denoted by red dotted circles) can be found in the microstructure of HB6. The dark gray contrast region (marked by a black arrow) associated with the B/C-rich phase is observed only in the case of HB6 (0.75 mol) (Figure S2c, Supplementary Information-II). In addition, the RHB5 specimen reveals oxide-free ceramic with a homogeneous distribution of constituent elements (Nb, Ti, Zr, Cr, C, and B) in the sintered microstructure, indicated by the corresponding elemental maps (see Figure S2d, Supplementary Information-II). It is worthwhile to mention that the occasional presence of elemental carbon could also be seen in some regions (indicated by blue arrows). The elemental compositions as estimated from the EDS measurements are listed in Table S1.

Fine-scale microstructural analysis

Extensive TEM investigation has been carried out on the RHB5 to obtain information on residual reaction product and their distribution along with the high-entropy boride (HEB) phase in the microstructure. Low magnification HAADF (high-angle annular dark field) imaging and corresponding TEM-EDS elemental maps have been obtained to ascertain the presence of various phases in the sample. Figure 3(a), (b) shows the HAADF micrograph of RHB5, indicating the formation of the HEB phase and their corresponding elemental maps [Fig. 3(b)], revealing the homogeneous distribution of constituent elements in the phase. The dark gray contrast region in the HAADF image belongs to residual carbon, as confirmed by the corresponding elemental map. In addition to this, a few other regions with elemental inhomogeneity are observed in Fig. 3(b), belonging to the residual oxide phase, i.e., Cr_2O_3. It is interesting that in spite of achieving a significantly high yield of the HEB phase, some remnant oxide phase and graphite are yet observed near the grain boundary of HEB phases. Detailed investigation of various portions of the sample is needed to confirm the presence of other residual phases in the microstructure.

We will further discuss how a combination of bright field images and selected area diffraction patterns can be used to identify residual phases in the sintered sample. Figure 4(a) shows a low magnification bright field TEM image, revealing [shown in Fig. 4(a)] the presence of residual reaction product at the grain boundary, within the gains as well as at the triple junction. The major phase belongs to a light gray contrast (indicated by a green arrow). The other contrast regions marked by arrows of different colors (red, deep yellow, and yellow arrows) indicate phases preferentially forming at the grain boundaries or

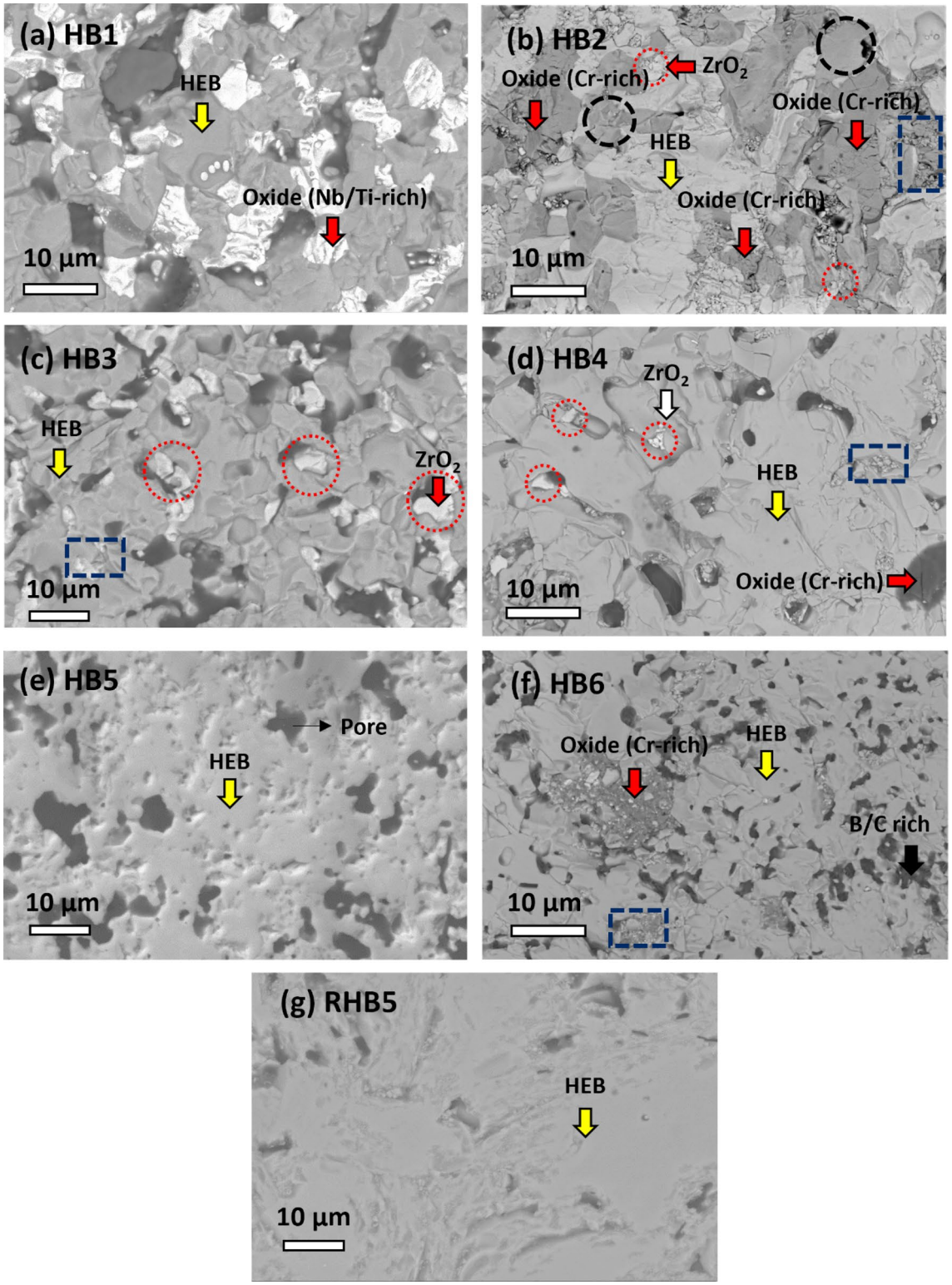

Figure 2: BSE-SEM micrographs of the spark plasma sintered pellets, showing the evolution of the high-entropy boride (HEB) phase (gray contrast regions) formed via boro-carbothermal reaction among different metal oxides (Nb_2O_5, TiO_2, ZrO_2, and Cr_2O_3) and various concentration of boron carbide (B_4C) (a) 0.45 mol; (b) 0.5 mol; (c) 0.6 mol; (d) 0.65 mol; (e) 0.7 mol; (f) 0.75 mol; (g) 0.7 mol (double sintered).

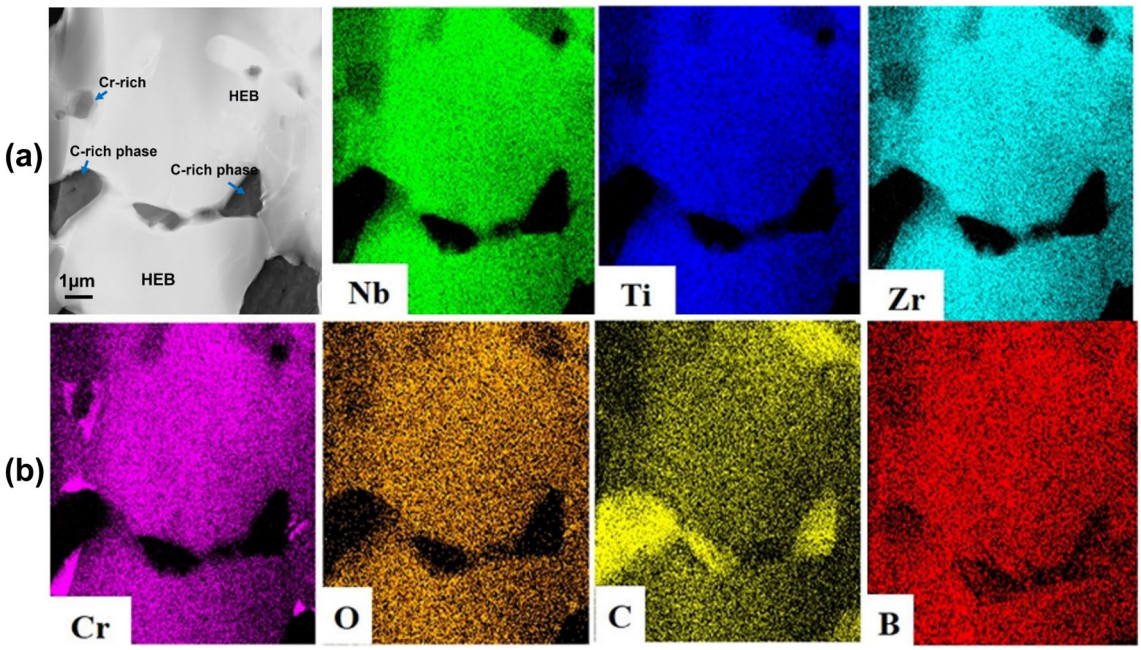

Figure 3: (a) HAADF image showing the distribution of different phases present in the RHB5 sample; (b) elemental maps showing the distribution of various elements, confirming the evolution of the high-entropy boride (HEB) phase.

interfaces between phases. Detailed finer-scale microstructure and their corresponding selected area diffraction (SAD) patterns have been acquired to confirm these phases. Figure 4(b) shows a high magnification bright field micrograph showing the triple junction formed by grains. The grains belong to the HEB phase, which is further confirmed by the SAD pattern [as shown in Fig. 4(b) lower inset]. Figure 4(c) shows another higher magnification bright field TEM micrograph, revealing two distinct phase contrasts of black and white. The upper left (4d) and lower left (4e) inset of Fig. 4(c) indicate SAD patterns corresponding to the white contrast phase within the HEB grain. The patterns can be indexed in correspondence with graphite (white contrast) and HEB phase (black contrast). The lower inset of Fig. 4(f) shows a microdiffraction pattern obtained from the black contrast area, revealing the presence of the $Nb_{0.8}Zr_{0.2}C$ phase. Figure 4(g) shows a higher magnification bright field micrograph from the two adjacent grain junctions of the HEB phase, revealing the presence of dislocation near the grain boundaries. The inset of Fig. 4(g) shows the composite SAD pattern acquired at the grain boundary. The pattern was indexed corresponding to the HEB grains. The brighter spots (indicated by the yellow arrow) confirm the HEB phase whereas the weaker spots (shown by the green line) reveal the formation of Cr_2O_3 at the grain boundary. Some grain boundaries between the HEB phase are found to be clean and devoid of any secondary phase. A high-resolution electron micrograph of the two adjacent HEB grains is shown in Figure S3, Supplementary Information-II. The FFT (Fourier Fast Transform) corresponding to two distinct points from the respective area is also shown in Figure S3 (b-c), respectively. Moreover, Fourier filtered image revealed that the *d*-spacing of both planes were almost the same, corresponding to the (110) plane of the HEB phase. This indicates the formation of a coherent interface between the two HEB grains.

Hardness and elastic modulus evaluation of HEB phase

The variation of hardness (H_v) and elastic modulus (E) of the HEB phase in the sintered pellets as a function of B_4C content is shown in Fig. 5. The microhardness values were measured using 0.5N load. Due to the presence of oxide phases in abundant amounts, the proper estimation of the hardness of the HEB phase in HB1 could not be done. The hardness for the HEB phase lies in the range of 32–37 GPa for the other sintered specimens. An abrupt increase in the hardness is observed at a B_4C content of 0.6 B_4C content, which subsequently remains almost unchanged. However, the variation in the elastic modulus for the sintered specimens shows a continuous increase with the increasing B_4C content from 0.5 mol. to 0.7 mol., lying in the range of 330–415 GPa. The highest value of hardness (36.8 GPa) is observed for the specimen containing 0.75 mol. B_4C while the highest value of elastic modulus (414.4 GPa) is observed for the resintered sample having a B_4C concentration of 0.7 mol. The variation of hardness is primarily due to phase purity or the chemical composition of the HEB phase. Since it is a multicomponent solid solution phase, the solid solution hardening dictates the hardness achieved. This, in turn, depends on

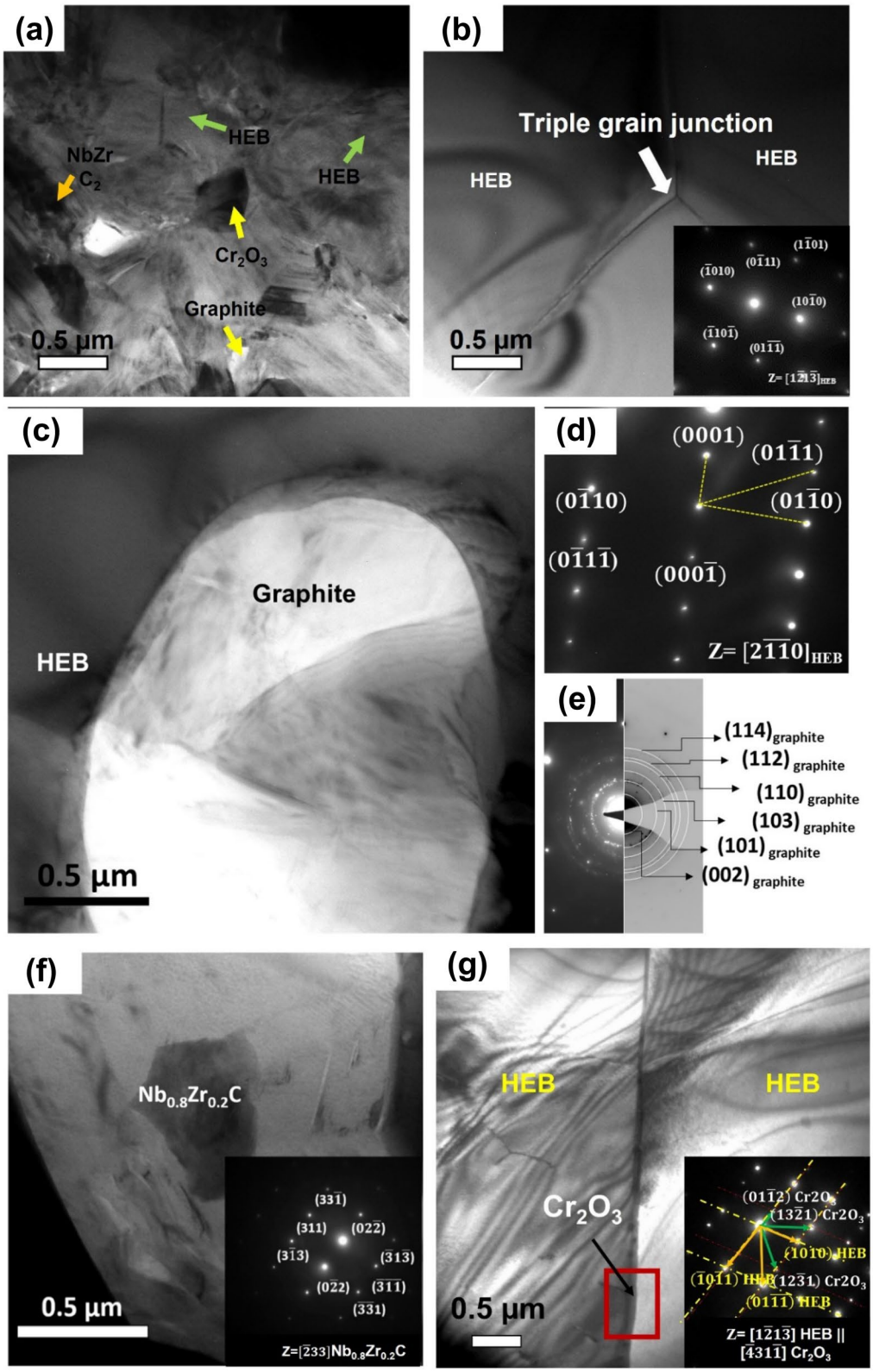

Figure 4: TEM bright field image of RHB5 showing (a) the presence of high-entropy boride (HEB), $Nb_{0.8}Zr_{0.2}C$, and remnant phases; (b) clean grain boundary and triple junction formed by three HEB grains. The inset exhibits the selected area diffraction pattern (SADP) from the HEB grain indicating the hexagonal structure; (c) presence of HEB phase and graphite as confirmed by the SADP obtained from (d) HEB grain, and (e) graphite. Bright field TEM images of RHB5 from another region show (f) the presence of remnant $Nb_{0.8}Zr_{0.2}C$ embedded in HEB grain, confirmed from the SADP (shown in the inset) acquired from dark contrast region; (g) grain boundary between two adjacent HEB grains. SADP (in the inset) corresponds to the region enclosed by a rectangular box, indicating the presence of the Cr_2O_3 phase.

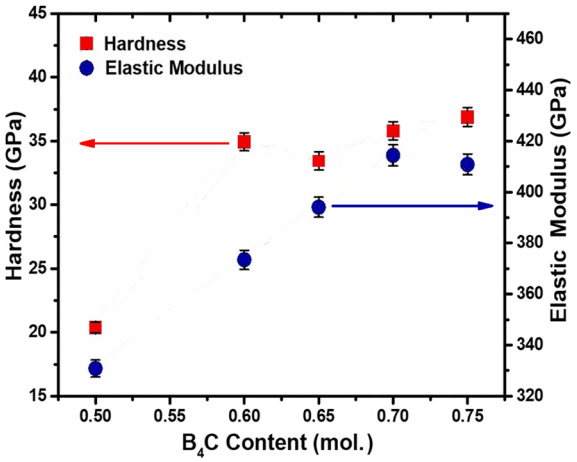

Figure 5: The variation in hardness and elastic modulus of the sintered pellets as a function of boron carbide (B_4C) content.

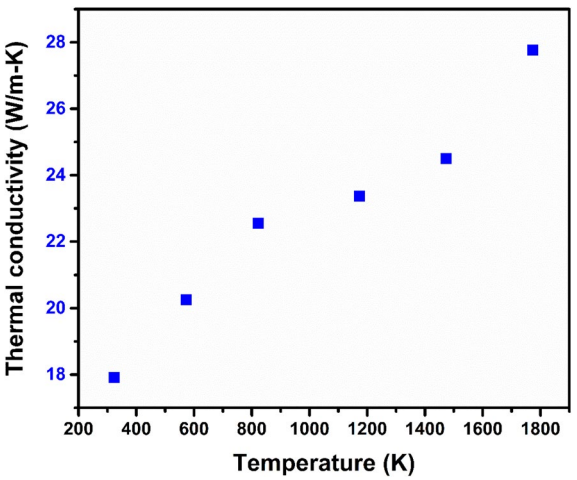

Figure 6: The variation in thermal conductivity of the near-fully formed quaternary diboride (RHB5) pellet at different temperatures.

the B_4C concentration used during sintering as the achievable amount of HEB phase is dependent on the B_4C concentration in the pre-sintered mix. The elastic modulus, on the other hand, depends on the type of M-B bond, which is the strongest in a multicomponent system. In either case, the contribution of the low-fraction phases (such as $Nb_{0.8}Zr_{0.2}C$ in RHB5, or B_4C in HB6) toward achieving higher mechanical values cannot be neglected. A brief comparison with the results from previous reports is listed in Table S2, Supplementary Information-II.

Thermal conductivity measurement of the bulk resintered specimen

The thermal conductivity of the RHB5 is presented in Fig. 6. Additionally, the thermal diffusivity and specific heat capacity are provided in Table S3, Supplementary Information-II. The RHB5 specimen shows thermal conductivity of 17.91 W/m K at room temperature. However, the thermal conductivity of this HEB is found to follow an ascending trend with temperature. The highest thermal conductivity achieved for the HEB phase in RHB5 is 27.77 W/m–K at 1800 K. It should be noted that that the near-room temperature thermal conductivity of this multicomponent boride is less than that of the binary compounds of some of the constituents such as (Zr, Ti)B_2 (87 W/m–K), and (Zr, Nb)B_2 (74 W/m–K) [34]. This low thermal conductivity may be due to the formation of high-entropy lattice, causing the major scattering of phonons by lattice distortion. Further, at high temperatures, pores present within the HEB phase can also act as a heat transfer medium, which can increase the thermal diffusivity. As a result, thermal conductivity may escalate at higher temperatures.

Discussion

The current investigation reports the synthesis of a multicomponent diboride from the individual oxides at a relatively lower temperature (< 2000 °C) using Reaction-aided Spark Plasma Sintering (RSPS) via the boro-carbothermal route. The Reaction-aided Spark Plasma Sintering (RSPS) provided an excellent alternative route compared to the conventional SPS of the constitutional diboride powder. The RSPS can avoid the time-consuming pre-sintering process, which involved severe mechanical treatment of the constituent boride powder that resulted in the presence of impurities from milling equipment in the powders. The starting materials being oxides bypass the common challenges, often faced during the synthesis of the bulk high-entropy diborides from the individual diboride powder. Subsequently, a study on the phase assemblage and detailed microstructural investigation of the reaction-sintered products revealed the maximum yield in the percentage of the HEB phase (~ 94%) in the RHB5 sample. However, fine-scale investigation of the RHB5 specimen reveals the presence of a few remnant phases within the HEB grains as well as grain boundaries, which could have evolved during the reactive synthesis of HEB via boro-carbothermal reduction of oxides by B_4C.

According to the comprehensive microstructural analyses, the reactive synthesis of HEB by boro-carbothermal reduction of the oxides is likely to be a two-step process. The first is interface-controlled, and it encourages the creation of individual diborides as a result of the interaction between the corresponding oxides and B_4C. Following that, HEB is formed via a diffusion-controlled pathway, with interdiffusion among the different individual diborides, playing a major role in HEB formation. Figure S4 (see Supplementary Information-II) depicts both processes in schematic form. The individual oxides and B_4C react at the interface via various intermediate reactions and form respective diborides. During the prolonged heating, the

individual diborides start to diffuse into each other and a new solid solution phase of a similar crystal structure is evolved due to the possible intermixing at elevated temperature, as shown in the inset of Figure S4b.

We shall now discuss the formation of the HEB via reactive SPS process from the viewpoint of both the interface-controlled and diffusion-controlled pathways. The thermodynamics of solid solution formation and the evolution of several intermediate reaction products are discussed for the interface-controlled path to provide insight into the boro-carbothermal reaction of the mixed oxides. The diffusion-controlled process is discussed based on a simple diffusion model, which has been simulated to provide a correlation between computational and experimental results. In addition, the reasons behind the retention of several secondary phases are also discussed from a thermodynamic aspect to provide insight into the boro-carbothermal reduction of mix-oxides.

Thermodynamics of solid solution formation

The formation of high-entropy boride (HEB) from a mixture of oxide is essentially governed by the thermodynamics of the boro-carbothermal reaction. However, the path of the boro-carbothermal reaction of mix-oxides is not the same as that of a single metal oxide. This reaction in a mixture of oxides can take place simultaneously or one after the other at a higher temperature (1800 °C in the present case). Thus, to explore the diffusion mechanisms and possible chemical reactions between the oxides and B_4C with/without C involved in the formation of the high-entropy boride phase, a thermodynamic analysis has been carried out using FactSage software. The possible reaction pathways (termed as R1–R4) and standard Gibbs free energy ($\Delta G_{reaction}$) of the formation of individual diboride (i.e., TiB_2, ZrB_2, CrB_2, and NbB_2, respectively) have been calculated as a function of temperature. For ease of comparison, the calculation for a suitable pathway of reaction between B_4C and mix-oxides (R5) is also provided. The details of the calculations are provided in S3, Supplementary Information-I. $\Delta G_{reaction}$ as a function of T is plotted for all the reactions and is shown in Figs. 7(a) and (b). The thermodynamic assessment provides the feasibility of the reduction of the transition metal oxides by B_4C to form the individual boride. It is worthwhile to mention that R5 has the lowest standard Gibbs free energy (ΔG) among all the reactions, indicating that R5 is the best possible pathway for obtaining HEB via the boro-carbothermal route. Thorough thermodynamic investigations of the intermediary processes can reveal the underlying likelihood for the existence of remnant phases such as $Nb_{0.8}Zr_{0.2}C$ and graphite in the sintered microstructure. Figure 7(b) depicts a representative plot of $\Delta G_{reaction}$ vs. T revealing the probable intermediate reactions between oxides and B_4C with the aforementioned stoichiometry, involving the creation of the intermittent carbide phase as well as transition metal diboride. The details of the calculations are provided in S4, Supplementary Information-I.

The negative values of $\Delta G_{reaction}$ of the initial reactants suggest the feasibility of boro-carbothermal reaction above 1200 °C in a spontaneous manner. This asserts the formation of complex oxide phases at high temperature as diffusion between the reactant oxides is also possible. However, it is very unlikely for all the respective metal oxides to undergo reduction at the same temperature. This reduction in temperature increases Nb_2O_5, Cr_2O_3, TiO_2, and ZrO_2 in ascending order. Considering the reduction of ZrO_2 becomes thermodynamically feasible at a much higher temperature [above 1200 °C, see Fig. 7(a)], ZrO_2 will likely react at a much slower rate during the initial phases as compared to

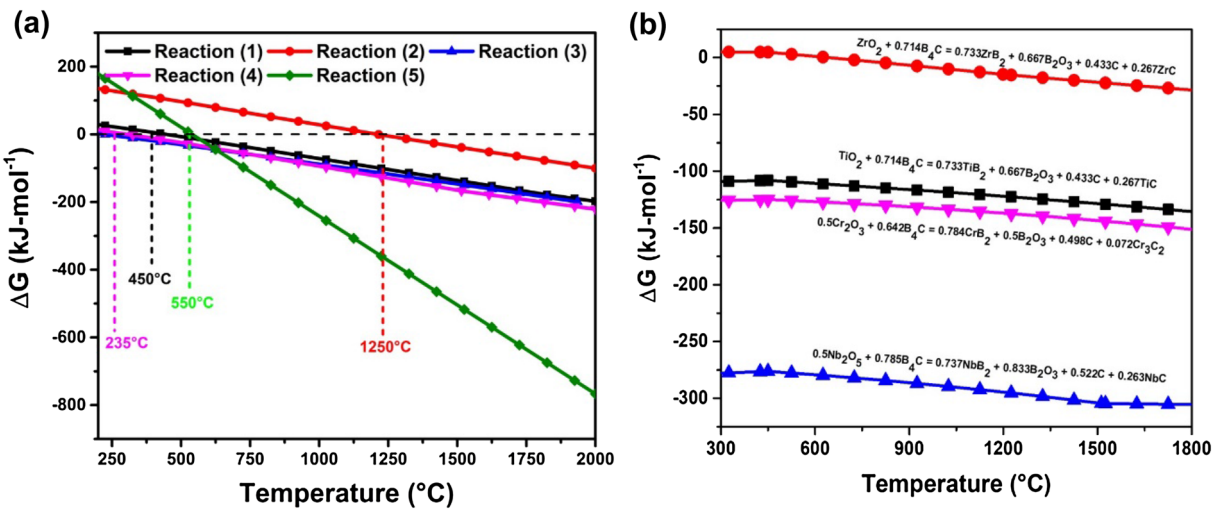

Figure 7: (a, b) Graphical representation of Gibbs free energy (ΔG) as a function of temperature obtained through commercially available FactSage software showing the feasibility of formation of different borides via boro-carbothermal reaction of oxides.

the other oxide reactants. The effect of such a delayed reaction is reflected in several experimental specimens where B_4C content is lesser than the optimum concentration (0.7 mol.) in the corresponding as-milled powder mixture HB1 to HB4. Traces of ZrO_2 can be observed in both the XRD pattern [Fig. 1(a)] and SEM micrographs](Fig. 2) of the corresponding sintered samples. On the contrary, when the amount of B_4C is increased in the milled mixture up to the optimum concentration (0.7 mol.) or more than that, the scarcity of the reducing agent for remnant ZrO_2 can be compensated. This is well reflected in the XRD pattern of HB5 and HB6, where peaks corresponding to the unreacted ZrO_2 have gradually disappeared, indicating a further reduction of the remnant oxide (see Fig. 1). It is worthwhile to mention that, irrespective of B_4C concentration in the milled mixture, the high-entropy boride (HEB) is present as the major phase. This can be explained by the nominal reaction pathway R5. At any stoichiometric condition, if the reaction occurs via R5, the standard Gibbs free energy of the reaction for the system is the lowest. Thus, it stabilizes the HEB phase as compared to other primary or secondary diborides that are formed at 1800 °C. As a result, the high-entropy boride (HEB) phase is obtained as the major phase in all the sintered specimens, while the other diborides appear as the minor phases (as shown in Fig. 2).

Furthermore, the particle size of the initial reactants has a significant impact on the production of individual diborides near the oxide-boron carbide contact. Smaller particles have a higher surface area than larger particles, increasing the total rate of the reaction along the contact/interfaces (here grain boundary regions). However, agglomeration in the reactant powder can stifle the reactions, leaving the possibility of residual oxides near grain boundaries or interfaces. Under such consideration, the fine-scale microstructural investigation was carried out near the grain boundaries of two adjoint HEB grains. This reveals the presence of Cr_2O_3 near the grain boundary of the HEB phase in the RHB5 sample [see Fig. 4(g)]. This can be attributed to the presence of large agglomerated Cr_2O_3 particles (particle size ~ 1 μm) (see Figure S1b, Supplementary Information-II) in the as-milled mixture, which could not be measured using DLS due to the sedimentation of large particles due to gravity. A larger particle size resulting in a smaller surface area is expected to make the rate of BCTR reaction between oxides and B_4C sluggish [28].

As the thermodynamic analysis shows that spontaneous reactions of all the oxides are possible, it is also true that the rate of the reactions for each oxide should be different. The rate constants play a major role in determining in which order the individual boride is expected to form in the reaction mixture. In this regard, the $\ln(k_{eq})$ vs. Temperature was plotted and shown in Figure S3a, Supplementary Information-I. The analysis indicates that the reactivity of Nb_2O_5 is fairly high in comparison with the other oxides, ensuring the prior formation of NbB_2 over other diborides. Although the rate of the reaction for the formation of NbB_2 decreases with increasing temperature, it remains sufficiently higher than the other three. Conversely, the equilibrium rate constants for the other three oxides show an increasing trend with increasing temperature. This signifies that the borocarbothermal reaction of these oxides is easily facilitated at elevated temperatures. However, in the temperature region above 1200 °C, the rate of change in $\ln(k_{eq})$ value is higher for ZrO_2 (from 0.034 to 5.196) compared to Cr_2O_3 (from 9.136–10.909) and TiO_2 (from 8.167 to 10.512). This sudden increase in the equilibrium rate constant can increase the localized reactivity of ZrO_2 with B_4C. Due to this fact, the rate of the forward reaction becomes higher at elevated temperatures. During the spark plasma sintering, the temperature at the interface between particles reaches very quickly due to the higher heating rate. Under such conditions, a sudden increment in the reactivity can cause rapid consumption of B_4C by ZrO_2, thus creating a possibility of localized deficiency of B_4C near the interface. In the absence of boron carbide, the reduction reaction cannot proceed further. Thus, the possible chance of a minute amount of any unreacted oxides being present in the grain boundary region is finite.

Computational representation of the diffusional transformation of high-entropy boride phase

As previously indicated, the generation of high-entropy boride from a combination of oxides is governed by both the interfacial reaction and the diffusional stages. The creation of the solid solution phase from individual diborides will be discussed further in the current section from a diffusional standpoint. In the earlier section, we have discussed that Nb_2O_5 has the highest rate of conversion from oxide to diboride via the borocarbothermal reaction pathway, while it is the lowest in the case of ZrO_2. Thus, by the time other oxides are converted fully into corresponding diborides, it is highly likely for NbB_2 to be already present in the system. If sufficient time is provided to allow diffusion, the other diborides will slowly diffuse into NbB_2 while replacing the parent Nb atom, thus finally obtaining near equilibrium concentration. However, the diffusion will preferably be decided by the size difference, i.e., smaller atoms are likely to diffuse faster than the atoms having relatively bigger ionic radii [35]. This, in turn, indicates that the smallest sized atoms will have a higher interdiffusion coefficient. Among all the components, zirconium has the highest ionic radii (0.72 Å) whereas chromium has the lowest (0.52 Å). Thus, it is expected that Cr will diffuse faster than Zr in Nb.

For a better representation of this intermixing process and diffusional formation of the HEB phase, a simple computational study was performed to generate the composition profiles of each component for the current system, i.e., (Nb, Ti, Zr, Cr) B_2. The details of the diffusional modeling (assumptions, initial

and boundary conditions) are provided in S5, Supplementary Information-I. The composition profiles are represented in Fig. 8. Figure 8a represents a concentration profile for binary diffusion between NbB_2 and CrB_2 whereas Fig. 8b represents the concentration profile of each component of the quaternary composition. For it, the maximum difference in the position of the interface for all components is less than 0.1 μm, validating our assumption of constant molar volume during the diffusion. From Fig. 8b, it can be observed that the crossover composition in mol.% is (25 Nb, 25 Cr, 25 Ti, 25 Zr), which is the equilibrium composition for the high-entropy solid solution phase as observed from the experimental evidence.

Conclusion

In the present investigation, bulk multicomponent high-entropy boride ceramics of $Nb_{0.25}Ti_{0.25}Zr_{0.25}Cr_{0.25}B_2$ have been successfully synthesized via a boro-carbothermal route from an oxide mixture using SPS at 1800 °C for 75 min. The effects of boron carbide addition on the evolution of the HEB phase have been examined through detailed microstructural investigation and corresponding thermodynamic analyses. The following conclusions can be drawn:

I. Experimental observations reveal that the volume fraction of the HEB phase increases with increasing the B_4C content in the powder mix. A maximum yield of 94% HEB is obtained at a B_4C content of 0.7 mol., in the double-sintered specimen (RHB5).
II. HAADF image and TEM-EDS elemental maps reveal the homogeneous distribution of the elements in the sintered microstructure of RHB5, indicating the formation of an almost fully developed HEB phase.
III. The presence of graphite and traces of intermediate carbides in the resintered sample can be attributed to the presence of an intermediate pathway for diboride formation through carbide and an incomplete reaction between the oxide mixture and boron carbide.
IV. The hardness and elastic modulus of the sintered specimens increases with increasing B_4C content, which is attributed to the increase in the volume fraction of the HEB phase in the sintered specimen. The maximum hardness of ~ 36.8 GPa is achieved for HB6 (containing 0.75 mol. B_4C) whereas the maximum elastic modulus of ~ 414 GPa is achieved for RHB5 (containing 0.7 mol. B_4C).
V. Thermodynamic and diffusional arrangement and calculations have been used to justify the formation of a multicomponent diboride phase.
VI. Thermodynamic calculations aid in predicting the temperature at which individual borides can be formed by boro-carbothermal oxide reduction. Due to the lack of a database of mixed borides and the requirement of interdiffusion coefficient between individual diborides, the formation temperature of HEB cannot be predicted.

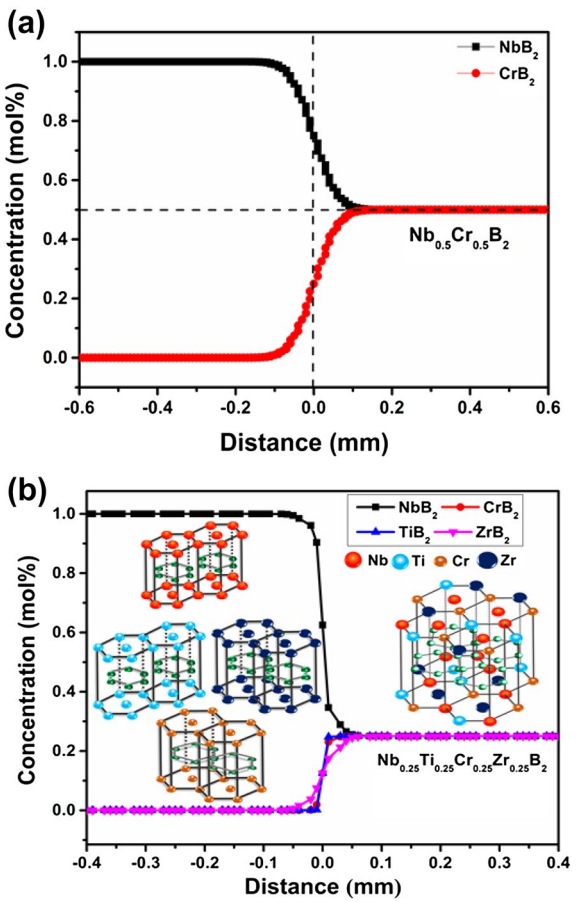

Figure 8: (a) Concentration profile for binary interdiffusion of CrB_2 in NbB_2. (b) Concentration profile for each component of the quaternary composition. The crossover composition as can be observed is $Nb_{0.25}Ti_{0.25}Zr_{0.25}Cr_{0.25}B_2$.

Experimental method

Powder processing and consolidation by SPS

For the preparation of bulk ceramics, commercially (AflaAesar, UK, Bhukhanvala Industries Pvt. Ltd. and SRL) available TiO_2 (particle size ~ 520 nm; purity ~ 99.995%), Nb_2O_5 (particle size ~ 770 nm; purity ~ 99.995%), ZrO_2 (particle size ~ 930 nm; purity ~ 99.9%), Cr_2O_3 (~ 325 nm, purity ~ 98 + %), and B_4C (~ 700 nm, purity ~ 98%) powders were used as initial reactant powders. Particle size reduction and mixing play a crucial role in catalyzing reaction kinetics and densification [36]. Thus, the oxide powders with equimolar ratio (calculated on the metal basis) were combined with varying concentrations of B_4C, and the powder batches were subsequently ball milled for 6 h at

60 rpm in a planetary ball mill (Pulverisette5, Fritsch, Germany) using zirconia milling media with a ball to powder weight ratio of 10:1. The compositions of the powders used to synthesize high-entropy boride (HEB), are listed in Table 1 and are marked as HB1 to HB6. Particle size distributions of the as-milled powders are provided in S6, Supplementary Information-I.

The as-milled powders were eventually consolidated into pellets of 15 mm diameter using the Spark Plasma Sintering machine (Dr. Sinter' 515 S, SPS Syntex Inc., Kanagawa, Japan). Our prior study indicated that NbB_2-based ceramics may be completely densified using a multistage sintering process at 1750 °C (with a total dwell time of 17 min), which is a lower temperature than previously reported [37]. Keeping this in mind, the multicomponent diborides [equimolar $(NbTiCrZr)B_2$ in the current work) were sintered at 1700 °C]. However, sintered density was poor with some of the reactants remaining. Hence, we increased the temperature by 100, 200, and 300 °C. However, a significant increase in the sintering temperature leads to grain growth and poor densification. Further as previously discussed promote the boro-carbothermal reaction, the powder is prepared in a vacuum furnace at 1600°–1650 °C at 10 °C/min for 60 min followed by sintering at 1900–2100 °C for 10–15 min to form bulk components. Hence, the reactive-SPS (RSPS) was carried out at a relatively lower temperature (1800 °C) for an increased dwell time (75 min) so that the reaction between oxides and B_4C is near complete, and densification is reasonably good. The heating was carried out with a heating rate of 100 °C/min. under the flow of Ar (2L/min) to promote the formation of HEB via boro-carbothermal reactions. As, RSPS is both a interface-controlled and a diffusion-controlled process, to facilitate a complete formation of the HEB phase via interdiffusion of the constituent diborides, a single-sintered sample can be further sintered using the same sintering cycle. This can be designated as resintering. A schematic diagram of the sintering profile for the formation of high-entropy borides via RSPS is shown in Figure S5 (Supplementary Information-II). The sintered pellet was ground and polished using different size grit paper (SiC paper: #80–2500) to obtain an asperity-free surface so that properties can be evaluated. A schematic representation of the overall procedure is depicted in Fig. 9. The room temperature bulk density of the sintered pellets was calculated using the Archimedes principle of buoyancy, where distilled water was used as a submersion medium by following ASTM B 962-17 standards and is shown in Table 1. As the initial phases and the final product phases in the sintered pellets are entirely different, thus, the estimation of relative density finds no relevance.

Characterization and thermodynamical calculations

Thermodynamic calculations using FactSage software were performed to predict the sequence, temperature stability, and possibility of boride formation due to boro-carbothermal reactions among the oxides and boron carbide. In addition to that, suitable diffusion modeling was also carried out to establish theoretical and experimental correlations. The phase determination of the as-received powder, powder mixture, as well as the sintered sample, was carried out using X-ray diffractometer (Empyron, Malvern Panalytical, Malvern, UK) using Cu-kα radiation (λ = 0.15404 nm) over the range of 2θ from 20° to 80°, at a step size of 0.013 and a scan rate of 0.022°/sec. The morphological and compositional characteristics of the pellets were determined using scanning electron microscopy (EVO 50, Carl Zeiss, Germany, and Nova NanoSEM-450, FEI, Netherlands) coupled with an energy-dispersive X-ray spectrometer (EDS, Oxford Instruments, UK). Further, the fine-scale and detailed microstructural features were observed by the combination of transmission electron microscope TEM (Techni: 20 UT, FEI, USA (operated at 120 kV) and Titan G2 60, FEI, USA (operated at 300 kV)).

TABLE 1: Composition of initial powders used to synthesize high-entropy boride phase.

Sample	Composition of the reactants in different powder mixtures (in mol)					Bulk density of sintered specimens (g/cm^3)	Relative density** (%RD)
	TiO_2	ZrO_2	Cr_2O_3	Nb_2O_5	B_4C		
HB1	0.25	0.25	0.125	0.125	0.45	5.062	~92.33
HB2	0.25	0.25	0.125	0.125	0.50	4.751	~86.66
HB3	0.25	0.25	0.125	0.125	0.60	4.912	~89.59
HB4	0.25	0.25	0.125	0.125	0.65	5.029	~91.73
HB5	0.25	0.25	0.125	0.125	0.70	5.000	~91.20
HB6	0.25	0.25	0.125	0.125	0.75	4.916	~89.67

**Relative density has been calculated with respect to the equimolar $(Nb, Ti, Zr, Cr)B_2$ phase. The theoretical density of the equimolar $(Nb, Ti, Zr, Cr)B_2$ phase is ~5.48 g/cm^3; calculated using the rule of mixture.

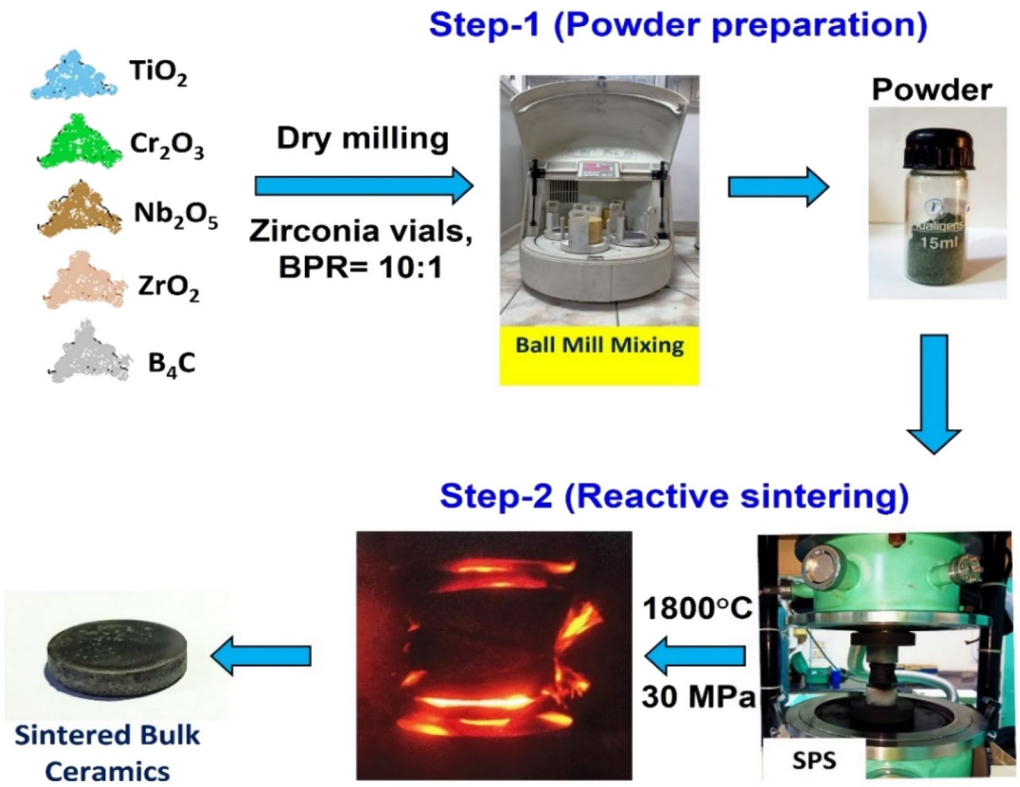

Figure 9: Flow diagram representing the synthesis procedure of bulk-(Nb, Ti, Zr, Cr)B_2 from the mixture of elemental oxides and B_4C via reactive spark plasma sintering.

Evaluation of mechanical properties using microindentation

The microhardness and the elastic modulus of the sintered pellets were measured under 0.5 N load (at a loading and unloading rate of 1000 mN/min with a dwell time of 15 s) using a Vickers microhardness tester (V-151, MHT, CSM Instruments, Switzerland) following ASTM C 1327-15 standard as expressed in the following expression:

$$H_V = (0.102)(1.8544)\left(\frac{P}{d^2}\right) \quad (1)$$

where H_V indicates the Vickers hardness in GPa, P is a load of indentation in N, *and d* is the average length of indent diagonals in mm. At least ten indents were taken to obtain a reliable hardness value for a sample. The reduced elastic modulus (E_r) was evaluated in GPa from the unloading curve (load vs. displacement) using the Oliver–Pharr method as expressed in the following equation [38],

$$E_r = \frac{1}{\beta}\frac{\sqrt{\pi}}{2}\frac{dP/dH}{\sqrt{A_p(h_c)}} \quad (2)$$

where β is a geometrical constant on the order of unity, $\frac{dP}{dH}$ is the slope of the load vs. displacement curve in N/mm, and A_pH_c is a fitting polynomial. Proper precautionary measures were taken to avoid the formation of cracks, spalling, or any kind of damage around the indent mark while indenting using Vickers indenter.

Evaluation of thermal properties

The thermal conductivity of the fully sintered specimen was measured indirectly using Laser Flash Apparatus (LFA 447 Nanoflash™ system, NETZSCH, Germany) under argon atmosphere (1 atm) following the ASTM 1461 standard (up to 1800 K). During the measurement, alumina was considered as a reference specimen. The Laser Flash Apparatus is often used to measure thermal diffusivity (α, in m^2/s) with related values of specific heat capacity (C_p, in J/kg-K) and density (ρ, in kg/m^3) values (which were measured using the Archimedes principle at room temperature) can be used to derive thermal conductivity (k, in W/m–K), according to the relationship:

$$k = \alpha \times \rho \times C_p \quad (3)$$

The measurements were conducted at 95% confidence with a coverage factor of $k = 2$.

Acknowledgments

We are immensely grateful to the Department of Science and Technology (DST India), and Science and Engineering Research Board (SERB) for their financial assistance toward fulfillment of this research work. We also thank Indian Institute of Technology, Kanpur for providing necessary assistance for the fulfillment of this work.

Funding

This study was supported by Department of Science and Technology (DST India), and Science and Engineering Research Board (SERB).

Data availability

Data will be made available on reasonable request.

Declarations

Conflict of interest The authors divulge any kind of interest on financial things.

Supplementary Information

The online version contains supplementary material available at https://doi.org/10.1557/s43578-023-00956-4.

References

1. B. Cantor, I.T.H. Chang, P. Knight, A.J.B. Vincent, Microstructural development in equiatomic multicomponent alloys. Mater. Sci. Eng. A. **375–377**, 213–218 (2004)
2. J.-W. Yeh, S.-J. Lin, T.-S. Chin, J.-Y. Gan, S.-K. Chen, T.-T. Shun et al., Formation of simple crystal structures in Cu-Co-Ni-Cr-Al-Fe-Ti-V alloys with multiprincipal metallic elements. Metall. Mater.Trans. A. **35**(8), 2533–2536 (2004)
3. A.S. Sharma, S. Yadav, K. Biswas, B. Basu, High-entropy alloys and metallic nanocomposites: processing challenges, microstructure development and property enhancement. Mater. Sci. Eng. R Rep. **131**, 1–42 (2018)
4. N.P. Gurao, K.J.C.S. Biswas, High-entropy materials: critical review and way forward. Curr. Sci. **118**(10), 1520 (2020)
5. J.W. Yeh, Recent progress in high entropy alloys. Ann. Chim. Sci. Mater. **31**, 633–648 (2006)
6. D.B. Miracle, O.N. Senkov, A critical review of high entropy alloys and related concepts. Acta Mater. **122**, 448–511 (2017)
7. M.-H. Tsai, J.-W. Yeh, High-entropy alloys: a critical review. Mater. Res. Lett. **2**(3), 107–123 (2014)
8. J. Gild, Y. Zhang, T. Harrington, S. Jiang, T. Hu, M.C. Quinn et al., High-entropy metal diborides: a new class of high-entropy materials and a new type of ultrahigh temperature ceramics. Sci. Rep. **6**(1), 37946 (2016)
9. Y.F. Ye, Q. Wang, J. Lu, C.T. Liu, Y. Yang, High-entropy alloy: challenges and prospects. Mater. Today. **19**(6), 349–362 (2016)
10. M. Qin, J. Gild, H. Wang, T. Harrington, K.S. Vecchio, J. Luo, Dissolving and stabilizing soft WB2 and MoB2 phases into high-entropy borides via boron-metals reactive sintering to attain higher hardness. J. Eur. Ceram. Soc. **40**(12), 4348–4353 (2020)
11. C.M. Rost, E. Sachet, T. Borman, A. Moballegh, E.C. Dickey, D. Hou et al., Entropy-stabilized oxides. Nat. Commun. **6**(1), 8485 (2015)
12. S. Jiang, T. Hu, J. Gild, N. Zhou, J. Nie, M. Qin et al., A new class of high-entropy perovskite oxides. Scripta Mater. **142**, 116–120 (2018)
13. D. Moskovskikh, S. Vorotilo, V. Buinevich, A. Sedegov, K. Kuskov, A. Khort et al., Extremely hard and tough high entropy nitride ceramics. Sci. Rep. **10**(1), 19874 (2020)
14. Y. Qin, J.-X. Liu, F. Li, X. Wei, H. Wu, G.-J. Zhang, A high entropy silicide by reactive spark plasma sintering. J. Adv. Ceram. **8**(1), 13 (2019)
15. J. Gild, J. Braun, K. Kaufmann, E. Marin, T. Harrington, P. Hopkins et al., A high-entropy silicide: (Mo0.2Nb0.2Ta0.2Ti0.2W0.2)Si2. J Materiomics **5**(3), 337–43 (2019)
16. P. Sarker, T. Harrington, C. Toher, C. Oses, M. Samiee, J.-P. Maria et al., High-entropy high-hardness metal carbides discovered by entropy descriptors. Nat. Commun. **9**(1), 4980 (2018)
17. T.J. Harrington, J. Gild, P. Sarker, C. Toher, C.M. Rost, O.F. Dippo et al., Phase stability and mechanical properties of novel high entropy transition metal carbides. Acta Mater. **166**, 271–280 (2019)
18. X. Yan, L. Constantin, Y. Lu, J.-F. Silvain, M. Nastasi, B. Cui, (Hf0.2Zr0.2Ta0.2Nb0.2Ti0.2)C high-entropy ceramics with low thermal conductivity. J. Am. Ceram. Soc. **101**(10), 4486–91 (2018)
19. E. Castle, T. Csanádi, S. Grasso, J. Dusza, M. Reece, Processing and properties of high-entropy ultra-high temperature carbides. Sci. Rep. **8**(1), 8609 (2018)
20. B. Ye, C. Fan, Y. Han, M. Ma, Y. Chu, Synthesis of high-entropy diboride nanopowders via molten salt-mediated magnesiothermic reduction. J. Am. Ceram. Soc. **103**(9), 4738–4741 (2020)
21. P.H. Mayrhofer, A. Kirnbauer, P. Ertelthaler, C.M. Koller, High-entropy ceramic thin films; a case study on transition metal diborides. Scr. Mater. **149**, 93–97 (2018)
22. Y. Zhang, W.-M. Guo, Z.-B. Jiang, Q.-Q. Zhu, S.K. Sun, Y. You et al., Dense high-entropy boride ceramics with ultra-high hardness. Scr. Mater. **164**, 135–139 (2019)

23. G. Tallarita, R. Licheri, S. Garroni, R. Orrù, G. Cao, Novel processing route for the fabrication of bulk high-entropy metal diborides. Scr. Mater. **158**, 100–104 (2019)
24. Y. Zhang, Z.-B. Jiang, S.-K. Sun, W.-M. Guo, Q.-S. Chen, J.-X. Qiu et al., Microstructure and mechanical properties of high-entropy borides derived from boro/carbothermal reduction. J. Eur. Ceram. Soc. **39**(13), 3920–3924 (2019)
25. J. Gu, J. Zou, S.-K. Sun, H. Wang, S.-Y. Yu, J. Zhang et al., Dense and pure high-entropy metal diboride ceramics sintered from self-synthesized powders via boro/carbothermal reduction approach. Sci. China Mater. **62**(12), 1898–1909 (2019)
26. B. Jiang, Y. Yu, J. Cui, X. Liu, L. Xie, J. Liao et al., High-entropy-stabilized chalcogenides with high thermoelectric performance. Science **371**(6531), 830–834 (2021)
27. L. Feng, W.G. Fahrenholtz, G.E. Hilmas, Two-step synthesis process for high-entropy diboride powders. J. Am. Ceram. Soc. **103**, 724–730 (2020)
28. H. Yuan, J. Li, Q. Shen, L. Zhang, In situ synthesis and sintering of ZrB_2 porous ceramics by the spark plasma sintering–reactive synthesis (SPS–RS) method. Int. J. Refract. Met H. **34**, 3–7 (2012)
29. L. Feng, W.G. Fahrenholtz, G.E. Hilmas, Processing of dense high-entropy boride ceramics. J Eur Ceram Soc **40**, 3815–3823 (2020)
30. D. Liu, H. Liu, S. Ning, B. Ye, Y. Chu, Synthesis of high-purity high-entropy metal diboride powders by boro/carbothermal reduction. J. Am. Ceram. Soc. **102**, 7071–7076 (2019)
31. J. Gild, A. Wright, K. Quiambao-Tomko, M. Qin, J.A. Tomko et al., Thermal conductivity and hardness of three single-phase high-entropy metal diborides fabricated by borocarbothermal reduction and spark plasma sintering. Ceram. Int. **46**, 6906–6913 (2020)
32. Y. Yang, J. Bi, K. Sun, L. Qiao et al., Novel (Hf0.2Zr0.2Ta0.2V0.2Nb0.2)B2 high entropy diborides with superb hardness sintered by SPS under a mild condition. Ceram. Int. **48**, 30859–30867 (2022)
33. L. Feng, F. Monteverde, W.G. Fahrenholtz, G.E. Hilmas, Superhard high-entropy AlB2-type diboride ceramics. Scr. Mater. **199**, 113855 (2021)
34. D. McClane, W. Fahrenholtz, G. Hilmas, Thermal properties of (Zr, TM)B2 solid solutions with TM = Hf, Nb, W, Ti, and Y. J. Am. Ceram. Soc. **97**, 1552 (2014)
35. C.-W. Cheng, C. Shih, R. Behera, W.-D. Hsu, Investigation of initial stages of nano-ceramic particle sintering using atomistic simulations. Surf. Coat. Technol. **231**, 316–322 (2013)
36. S.S.N. Murthy, M. Patel, J. Reddy, V.V. Prasad, Influence of B_4C particle size on the synthesis of ZrB2 by boro/carbothermal reduction method. Trans. Indian Inst. Met. **71**, 57–65 (2018)
37. T. Maity, K. Biswas, B. Basu, Critical role of ZrO_2 on densification and microstructure development in spark plasma sintered NbB_2. Acta Mater. **152**, 215–228 (2018)
38. W.C. Oliver, G.M. Pharr, Measurement of hardness and elastic modulus by instrumented indentation: advances in understanding and refinements to methodology. J. Mater. Res. **19**(1), 3 (2004)